

An Asymmetric Spoof-Fluid-Spoof Acoustic Waveguide and its Application as a CO₂ Sensor

Nathan Perchikov¹, Đorđe Vujić¹, Branimir Bajac¹, Andrea Alù², Vesna Bengin¹, and Nikolina Janković¹

¹ BioSense Institute, University of Novi Sad, Serbia

² Advanced Science Research Center, City University of New York, New York, USA

*To whom correspondence should be addressed: nathan.perchikov@biosense.rs, nikolina@biosense.rs

Abstract

We study pressure acoustic propagation in asymmetric spoof-fluid-spoof acoustic waveguides and its potential application in acoustic gas sensors. First, a stable and efficient analytical method is established for fast calculation of the dispersion curves based on spectral expansion and enforcement of continuity between segments at suitable collocation points. The analysis is validated by a commercial finite element software. The geometric design of the waveguide is then optimized for the emergence of a nearly-flat dispersion curve associated with vertical geometric asymmetry. The waveguide is fabricated using 3D printing technology and the measurement results corroborate the numerical simulations. Based on the nearly-flat dispersion curve supported by this waveguide, a CO₂ sensor is proposed allowing to relate the phase difference measured between two points in the waveguide to the composition of the gas in the waveguide. The proposed sensor is experimentally validated in a controlled environment and the measurement results match the computational predictions well. The sensor is robust with respect to noise and signal-recording duration due to fast phase measurements and shows high sensitivity to gas concentration due to reliance on the second, nearly-flat, dispersion curve. In addition, the sensor is label-free and low-cost, while exhibiting rapid response, low-maintenance requirements and potential for measurements in a wide range of CO₂ concentrations without saturation issues.

Keywords

Acoustic waveguide, spoof plasmon polariton, gas sensor, spectral point-collocation analysis

1. Introduction

Periodic structures have been studied for decades, however only with the introduction of the concepts of phononic and photonic crystals and later metamaterials, have these structures unlocked their full potential allowing for almost arbitrary wave manipulation and the engineering of devices with novel functionalities [1-8]. Subwavelength unit cells and the presence of local resonances are the key features of metamaterials that provide properties radically different from those of conventional media. Owing to these features, spoof surface plasmon polaritons (SSPP), which emulate natural surface

plasmon polaritons albeit operating in other frequency ranges than the optical one, have been successfully developed [9-16].

Based on the same idea, acoustic SSPP have been realized at the interface of a fluid and a corrugated surface, exhibiting similar properties in terms of wave localization [17-21]. The phenomenon of acoustic SSPP has found a number of applications, including collimation of sound [22-24], bending of sound [25], extraordinary transmission [26], focusing [27-29], imaging [29], multiband propagation [30], rainbow trapping [31], filtering and sensing [32].

Recently, we studied an aSSPP waveguide that is a counterpart of a metal-insulator-metal plasmonic waveguide, i.e., a spoof-fluid-spoof (SFS) acoustic waveguide [33]. Although the structure has a potential for various applications, it should be noted that the SFS waveguide represented a symmetric case, in which the two surfaces had the same geometry. The performed experiments validated the dispersion characteristics of the first two modes as calculated, albeit without demonstrating any particular applications.

One of the applications for which acoustic structures show a great potential is gas sensing, which is critical for monitoring and detecting the concentration of hazardous gases, air quality, environmental protection, or general analysis across various industries, including safety, aerospace, life-science, and the medical, and agricultural industries [34-39]. The main advantages of acoustic structures when compared to other types of gas sensors are robustness, low maintenance, rapid response, and, generally, low cost.

The first acoustic gas sensors were based on speed-of-sound measurements and the associated sensing platforms were typically bulky, as they included acoustic pipes and large actuators and transducers [40-44]. Significant size reduction was achieved with sensors that employed piezoelectric materials and propagation of various surface (SAW) and bulk acoustic waves (BAW) such as the Rayleigh, Love, Lamb, bulk-longitudinal, thickness-shear, and thickness-extension modes [45-51]. While being very attractive due to their size and performance, such sensors usually require advanced fabrication technologies.

More recent types of acoustic sensors usually rely on periodic structures, the typical examples being phononic crystals [52-60] and spoof-plasmon-based sensors [61]. It should be said, however, that the majority of the proposed sensors were only studied analytically and numerically, never providing experimental verification, which is crucial for practical applications. Moreover, in most of the

studies the sensor-response is based on damped-resonance amplitude-change, rather than on phase-measurement. In addition, only the fundamental mode of the structure is utilized. Both choices limit the sensitivity potential. Another issue is that pressure-amplitude measurements are more susceptible to noise, when compared to phase measurements, and thus the latter can provide more robustness and reliability, even when lower modes are employed.

An advantageous alternative is the utilization of nearly-symmetric structures, in which the symmetry is associated with the possibility to excite perfectly-localized modes. Specifically, the higher-mode dispersion bands of nearly-symmetric periodic structures can be nearly-flat, which can provide high sensitivity of a sensor. In general, higher modes and the related flat bands have been widely investigated both in purely periodic structures and in periodic structures with defects [62-71], however, the utilization of these phenomena remained unexploited in sensing structures.

In this paper, we extend the concept of symmetric SFS waveguides to a general vertically-asymmetric case, in which the two bounding surfaces have different geometrical parameters. A thorough spectral point-collocation-based dispersion analysis along with finite-element analysis validation are presented. We show that one of the main advantages of such a structure, with the additional degrees of freedom, is the possibility to manipulate higher modes in a more flexible way. More concretely, the first higher mode can be tailored to have a nearly-flat dispersion diagram, which consequently produces a significant phase change even for minute changes in the surrounding fluid characteristics. Using this as the underlying idea, we propose a very sensitive acoustic gas sensor for the detection of CO₂. After the numerical analysis and the parametric optimization of it, the sensor is fabricated using low-cost 3D printing technology and then experimentally tested in a controlled environment. Besides being cheap and easily

fabricated, the proposed sensor has the advantage of rapid response without the need for recovery or maintenance, higher robustness and sensitivity when compared to other acoustic sensors as well as successful operation in a large gas-concentrations range.

To the best of our knowledge, this is the first sensor based on the concept of relating fluid characteristics to acoustic phase-difference measurements for waves excited at frequencies associated with the higher mode, with a corresponding nearly-flat dispersion band reflecting a small vertical perturbation of an horizontally-periodic structure. The proposed sensor can be further extended to perform with other types of analytes.

The structure of this paper is as follows: after the Introduction, in Section 2 and the associated Appendix A, we present the theoretical background and the employed computational framework, which includes point-collocation-based spectral analysis, as well as finite-element simulations. Section 3 exhibits experimental validation of the numerical results. Section 4 details how the proposed structure can be utilized for gas-sensing applications. Section 5 gives a thorough overview of the fabrication and measurements results for the proposed CO₂ sensor. Further comparative analysis of the quality and novelty of the sensor is given in Section 6. Section 7 concludes.

2. Theoretical Background

The layout of the proposed asymmetric spoof-fluid-spoof (ASFS) waveguide, along with the corresponding geometrical parameters, are shown in Figure 1. We consider lossless two-dimensional geometry with perfect rigid surfaces, the structure being invariant in the z direction and bounded in the y direction. The ASFS waveguide is vertically asymmetrical, consisting of two surfaces with corrugations that in a general case have different geometrical parameters but the same periodicity d and are separated by a gap g . The fluid that occupies

the structure is characterized by its density ρ and speed of sound C .

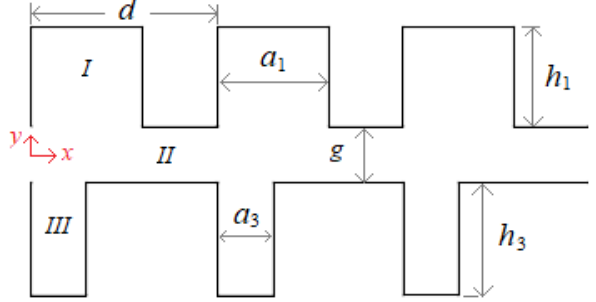


Figure 1: A 2D sketch of the asymmetric spoof-fluid-spoof waveguide.

There are two main computational approaches to obtain the dispersion diagram of the proposed structure. The first approach is finite element discretization with iterative solution of the associated linear eigenvalue problem combined with the mode-matching technique, where continuity conditions are enforced between the different rectangular segments in the waveguide in the integral sense, using projection on the basis-function space [72]. Another approach is the point-collocation method, following which continuity is enforced on a given set of discrete points [73].

The finite-element approach basically approximates the unknown functions using a basis of piece-wise linear functions with so-called local support [74]. The advantage of the finite-element approach is that increase in resolution does not automatically translate to increase in the condition number of the representative matrix of the eigenvalue problem associated with the dispersion analysis. On the other hand, special care has to be taken to avoid spurious (non-wave) solutions. In contrast, if one expands the unknown fields individually in each rectangular segment using a basis of wave functions, the physicality of the solution is guaranteed. However, due to the fact that waves are described by complex exponents, the approach suffers from certain numerical stiffness, since increase in resolution does directly translate to increase in the condition number of the matrix representing the continuity of

fields between the different segments. For instance, in [75] a mode-matching strategy was employed, entailed in projecting every basis function of the wave-equation kernel by use of a basis of similar wave functions, albeit with a different period, the ratio of the periods being dependent on the respective sizes of the rectangular segments comprising the waveguide periodicity-domain. Such an approach leads to very large representative continuity-enforcing matrices. Consequently, for highly asymmetric structures, the condition number of the representative matrix may become so high as to make the problem intractable on a regular processor.

In contrast, the present work proposes to employ the point-collocation strategy, as an alternative for the mode-matching technique, while remaining in the framework of the wave basis-functions approach. One disadvantage of the point-collocation approach is the high sensitivity of the solution to the choice of the collocation points. However, if a robust choice of points is suggested, the approach becomes advantageous. A detailed derivation of the dispersion equation using the point-collocation approach is given in Appendix A together with a thorough explanation related to the stability of the approach and the choice of the collocation points.

To validate the spectral analysis, dispersion diagrams for the proposed structure have also been obtained using the commercial finite-element program COMSOL Multiphysics using the two-dimensional pressure-acoustics frequency-domain eigenfrequency solver. Figure 2 shows a dispersion diagram for the first five modes obtained using the spectral-collocation and the finite-element methods for the ASFS structure with $a_1 = 10.3$ mm, $a_3 = 10.3$ mm, $d = 34.3$ mm, $g = 10.3$ mm, $h_1 = 18.2$ mm, $h_3 = 20.6$ mm, confirming excellent agreement between the two methods. Figures 3 and 4 show dispersion diagrams for the first two modes for the ASFS structure with $a_1 = 10.3$ mm, $a_3 = 10.3$ mm, $d = 34.3$ mm, $g = 10.3$ mm, where the parameters h_1 and h_3 are varied. The fluid in the structure has the

following parameters: $\rho = 1.1802 \text{ kg/m}^3$, $C = 346.8705 \text{ m/s}$.

Excellent agreement between the analytical and numerical results can be observed in Figure 2, confirming the validity of the chosen analytical approach. The fundamental mode exhibits the expected behavior where the slope of the flat part can be modulated by the change of the geometrical parameters.

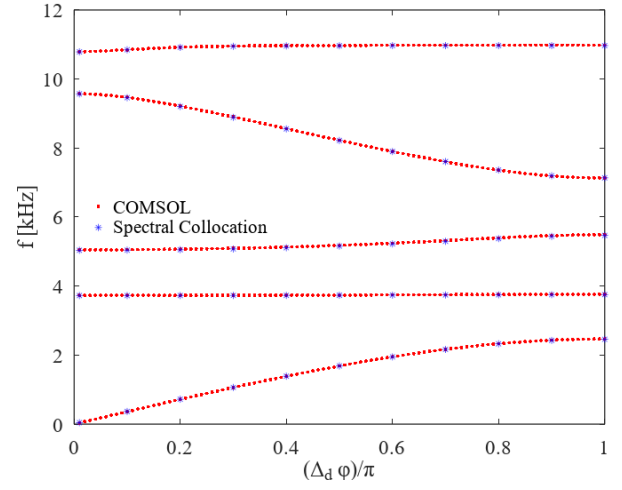


Figure 2: Dispersion diagram of the first five modes for $a_1 = a_3 = g = 10.3$ mm, $d = 34.3$ mm, $h_1 = 18.2$ mm, $h_3 = 20.6$ mm, obtained using the spectral-collocation and the finite-element methods.

However, of particular interest is the second mode, since the asymmetry in the structure enables flexible manipulation of its slope. In other words, the configuration can be used to tailor the second mode to be nearly-flat, i.e., to have slow-wave nature yet enabling propagation and such a property can be of a great advantage in the design of a sensor because it can provide fast sensing and high sensitivity.

In other words, in the scenario of quasi-flatness and a sensing principle based on a phase change, a minute change of a fluid parameter would not change the *shape* of the dispersion diagram, but it would slightly push it towards higher frequencies. Measured at a specific frequency, the signals before and after the minute change in the fluid would have significantly different wavenumbers. This is the basic

idea of the sensor, which will be elaborated on in the following.

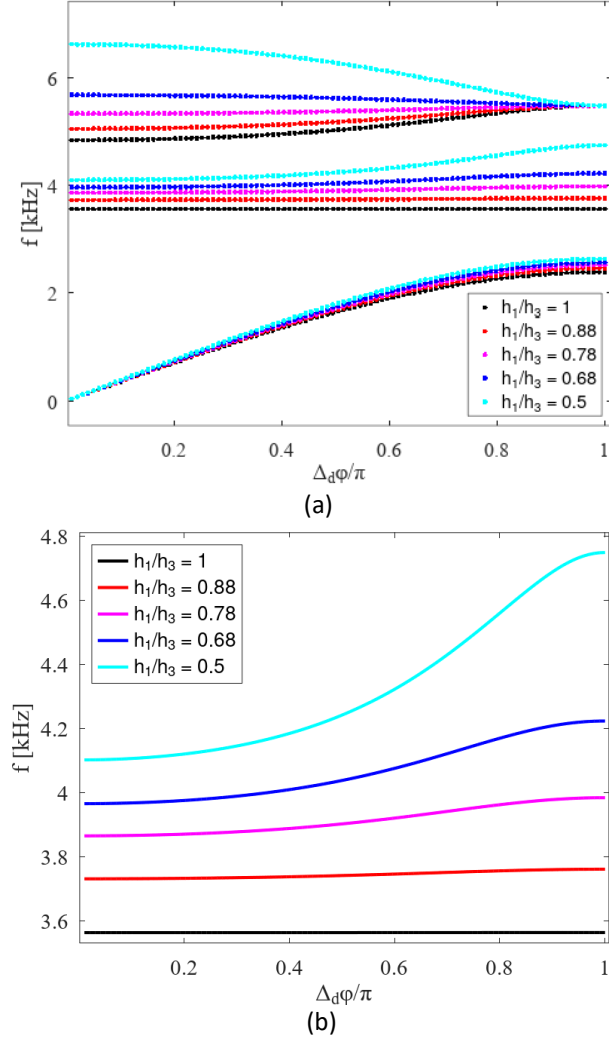


Figure 3: Dispersion diagrams of the first three modes (a) and a zoom-in on the second mode (b) for $a_1 = a_3 = g = 10.3$ mm, $d = 34.3$ mm, $h_3 = 20.6$, and various $h_1/h_3 < 1$ values.

We observe from comparing Figures 3(a) and 4(a) that vertical perturbation of the symmetry is a higher-order effect than the horizontal perturbation. Both effects are small, and small perturbation does not affect the first mode much. But a small change in h_1/h_3 gives a large change already in the *second* mode dispersion curve, whereas a small change in a_3/a_1 gives a large change only in the *third* mode of the dispersion curve.

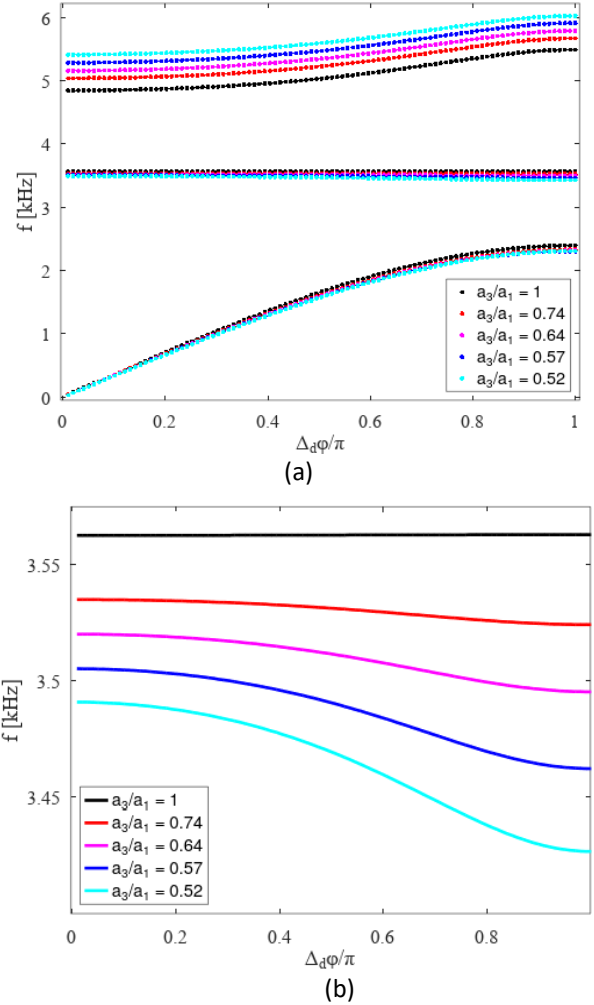


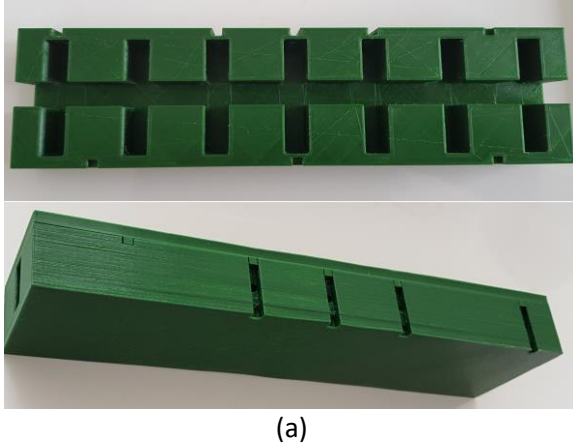
Figure 4: Dispersion diagrams of the first three modes (a) and a zoom-in on the second mode (b) for $h_1 = h_3 = 20.6$ mm, $g = 10.3$ mm, $d = 34.3$ mm, $a_3 = 10.3$, and various $a_3/a_1 < 1$ values.

This suggests that using a vertical perturbation would be technologically easier, since the response sensitivity is of higher order. In addition, one notes that the group velocity that can be associated with the second mode is negative for a horizontal perturbation. This means that detection of the second-mode wave propagation experimentally is expected to be more challenging for a horizontal perturbation. In view of this, the present study employed a vertical perturbation of the symmetry for the design of a sensor.

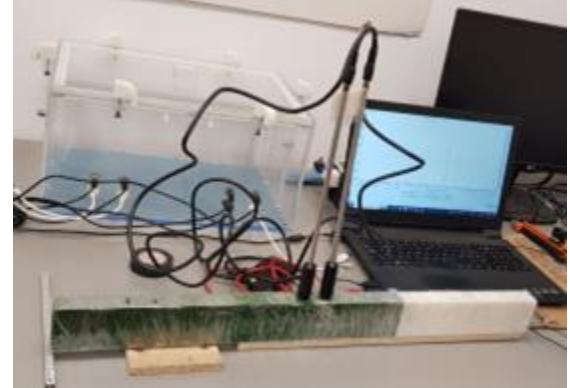
3. Experimental validation of the ASFS waveguide

In order to corroborate the analytical and numerical results, an ASFS waveguide prototype was fabricated using 3D-printing with a poly-lactic acid (PLA) filament employing a truss-like substructure for the solid parts of the structure of the waveguide. The geometrical parameters of the fabricated structure are $d = 34.3$ mm, $a_1 = a_3 = g = 10.3$ mm, $h_1 = 20.6$ mm, $h_2 = 18.2$ mm, and the width in the z direction is equal to 20 mm, while the fluid is air with the parameters $\rho = 1.1802 \text{ kg/m}^3$, $C = 346.87 \text{ m/s}$. Due to the need for a sufficient number of unit cells and, at the same time, the limitations of the 3D printer, three equal segments were fabricated separately, each comprised of 7 unit cells, as shown in Figure 5.

The three segments were attached to an aluminum profile and tightened for straight alignment and pressed against a commercial speaker attached to a sound blaster device connected to a laptop. Two small microphones were mounted with a distance d between them on the central segment, with the head of each microphone sunk into a drilled hole in the waveguide, allowing the microphone to perform as a probe of pressure inside the upper corrugation of the waveguide. A slow chirp signal with linear time-increase in frequency was created using the audio-analysis software Audacity [76] and played using the speaker. Consequently, the phase shift between the two microphones was measured and recorded.



(a)



(b)

Figure 5: (a) Fabricated segment of the ASFS waveguide, (b) Measurement setup.

The relative phase shifts and the corresponding applied excitation frequencies were used to obtain experimental dispersion diagrams. For the purpose of a better comparison of the simulated and measured results, a 3D model was created in COMSOL, and the corresponding dispersion curves were calculated. The comparison in Figure 6 reveals an excellent agreement between simulated and measured results.

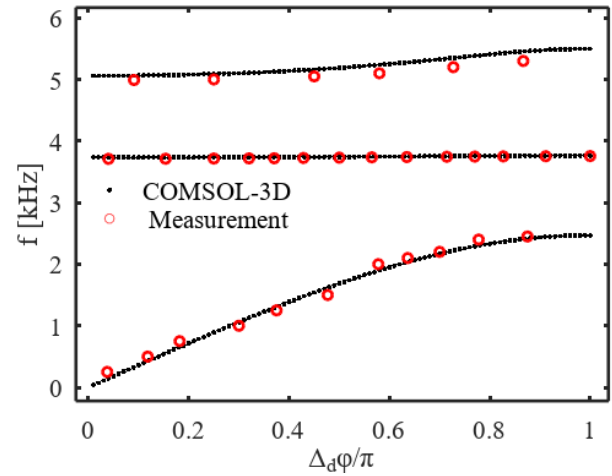


Figure 6: Comparison of calculated and measured dispersion curves for the ASFS waveguide.

4. A CO₂ sensor based on the ASFS waveguide

As discussed above, acoustic gas sensors typically rely on the fundamental modes of the acoustic structures, while the sensing principle is

predominantly based on the amplitude change of a signal. As it happens, however, amplitude measurements are typically prone to be corrupted by noise, although this can be mitigated to some extent [44]. This is one of the consequences of the fact that low-amplitude pressure measurement devices (microphones) are normally relative rather than absolute and can be affected by surrounding sounds of different frequencies. The amplitude of resonance in a higher mode is usually lower than in the fundamental mode, and hence it is rarely used for amplitude measurements. On the other hand, fundamental modes have a linear dispersion curve for most wavenumbers, which in principle challenges their utilization in sensitive large-range sensors. In contrast, due to their slow-wave property, nearly-flat-dispersion modes can be an excellent choice for high sensitivity sensing that is based on measuring phase changes. In this context, we demonstrate a novel sensor employing the second mode of an ASFS waveguide and a phase-measurement principle, aimed at the detection of the concentration of CO₂ in composition of air in the vicinity of the sensor.

Figure 7(a) shows the numerically obtained dispersion curves for an ASFS waveguide for various CO₂ concentrations. The geometric parameters were optimized such that the second mode appears around 11 kHz and their values are: $d = 11.5$ mm, $a_1 = a_3 = g = 3.5$ mm, $h_1 = 6$ mm, $h_3 = 6.9$ mm, and the width in the z direction is equal to 12.5 mm. The geometric-parameters values were decreased compared to the previously shown ASFS waveguide to correspond to a more compact structure and to match our fabrication and measurement capabilities, as detailed in the following section. The change in the CO₂ concentration was modeled in simulations through its effect on the values of the density ρ and speed of sound C of a mixture of the air and CO₂, using the following formulas:

$$\rho = \rho_{air}^{23^\circ C} \left[1 + \left(\frac{M_{CO_2}}{M_a} - 1 \right) c_v \right], C = \sqrt{\frac{1+2[(1-c_v)\alpha_{air}+c_v\alpha_{CO_2}]^{-1}}{1+\frac{2}{\alpha_{air}}}} \frac{C_{air}^{23^\circ C}}{\sqrt{1+\left(\frac{M_{CO_2}}{M_a}-1\right)c_v}}, \quad (1)$$

$$\frac{M_{CO_2}}{M_a} = \frac{44.01}{28.9647}, \alpha_{CO_2} = 6, \alpha_{air} = 5.003, \rho_{air}^{23^\circ C} = 1.192 \frac{kg}{m^3}, C_{air}^{23^\circ C} = 344.96 \frac{m}{s}. \quad (2)$$

where M_x denotes molecular weight of material x , and α is the number of degrees of freedom of a gas molecule. We note that CO₂ concentration of 0% means that the mixture consists of pure air, which includes 0.04% of CO₂. By the same token, CO₂ concentration of 1% means that there is 1.04% of CO₂ in the mixture, i.e., 1% of the CO₂ has been added.

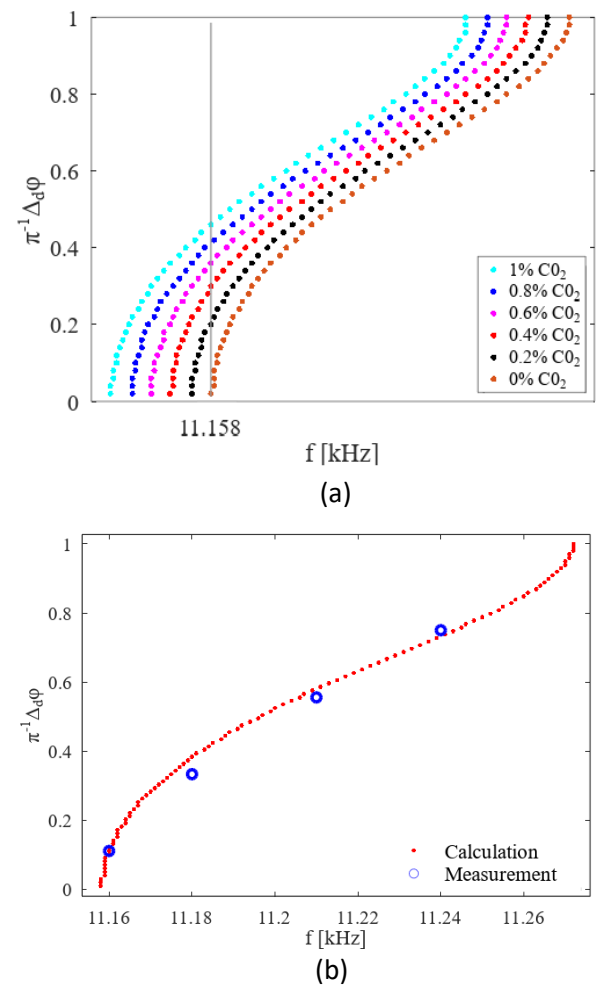


Figure 7: Calculated dispersion diagrams of the second mode of an ASFS waveguide for various concentrations of CO₂ (a) and validation of 0% CO₂ case against measurement (b).

One observes that the different dispersion curves have the same shape yet there is a slight red spectral

shift as the CO_2 concentration increases. The grey vertical line going through different-concentration dispersion curves for the frequency of 11.158 kHz shows how different concentrations cause different phase accumulations along the waveguide. It should be noted that the structure has to be cautiously optimized so that the second mode becomes only nearly flat (and not perfectly flat). Then, the mode would not represent a standing-wave excited at an isolated frequency value, but rather would enable slow wave propagation and allow the measurement of the phase change along the waveguide. Moreover, propagation can occur at a specific frequency for a whole range of values of a target analyte.

According to the performed numerical simulations, the proposed ASFS waveguide has a sensitivity of 0.003 Hz/ppm, which means that a concentration change of 300 ppm produces a 1 Hz shift in the frequency response. However, one should not be misled by sensitivity value since our sensor is based on the phase-change response to the concentration change, and in such a scenario the full phase range is adjusted to the prescribed range of CO_2 concentrations, while the frequency range is a consequence of the chosen concentrations range. Therefore, the overall sensitivity is equal to $\pi/\Delta c_v$, so it is smaller for a larger range of concentrations. Furthermore, the sensor utilizes nonlinear phase response, which allows for higher phase response to small concentration changes specifically at low concentrations. There, this sensitivity is not expressed in a high value of Hz per ppm, since we do not suggest measuring the frequency shift itself. Instead, we suggest measuring the phase shift, and indeed, we have a large value of phase shift per ppm of concentration for low concentration values. This high sensitivity is not manifested in a high value of a slope of a linear curve, but rather in the fact that the response is concave, and for low concentrations the (variable) slope becomes very high. This concave response is achieved by adjusting the operational frequency to have zero group velocity at the zero-phase limit.

A practical issue related to the resolution of the sensor is the following. In COMSOL calculations at frequencies around 10 kHz, the accuracy of the eigenvalue solver is 10^{-4} , which means 1 Hz frequency resolution, or 300 ppm concentration resolution. Also, for the actual sensor, in a measurement, the absolute sensitivity is lower: the maximum sampling frequency of a standard sound card is around 34 times the operational frequency chosen here, which implies 17 sampled points per half-period, or 1 sample point for 500 ppm. Therefore, it may be stated that the maximum possible absolute resolution of the sensor with standard electronic equipment would be around 500 ppm. The normal concentration of carbon dioxide in air is 400 ppm, which means that the design sensor is sufficient for detecting concentrations from the perspective of health hazards in inhalation.

Figure 7(b) shows open-air measurements with the sensor at various frequencies in the relevant range covering all the relevant phase range. One observes very good experimental validation of the calculations.

In the following section, the sensing principle is demonstrated experimentally, and the sensor's properties and performance are discussed in detail.

5. Experimental testing of the CO_2 sensor

To test the proposed sensor experimentally, the structure was fabricated using 3D printing technology, employing a PLA filament, and the acoustic response was measured for several relevant CO_2 concentration values in controlled environment. Prior to fabrication and measurements, several issues had to be resolved. Specifically, the dimensions and the quantity of the unit cells in the ASFS waveguide sensor were determined by the 3D-printer resolution (dictating the minimal geometric dimension in the waveguide), the size of the available microphones and size of the gas chamber available for the experiment; the necessity to have a sufficient number of unit cells to achieve a well-resolved wave structure and, ultimately, the desire

to have a more compact structure compared to the previously presented ASFS waveguide.

Several 3D simulations were run to determine the final configuration and geometric parameters, where the analyzed structures were comprised not only of the ASFS waveguide but also of holes for the microphones, which were modeled using radiative boundary conditions.

Dispersion diagrams for the optimized waveguide structure for different CO_2 concentrations were obtained following the principle explained in the previous section and using Eqs. (1) and (2), where the temperature was measured and set to 23 °C. Since the calculated dispersion diagrams turned out to be practically the same as for the initial structure, we will omit them here. The operating frequency was chosen to be 11.158 kHz. This value produces maximum measured-phase sensitivity at small concentrations and enables covering the full range of relevant CO_2 concentrations.

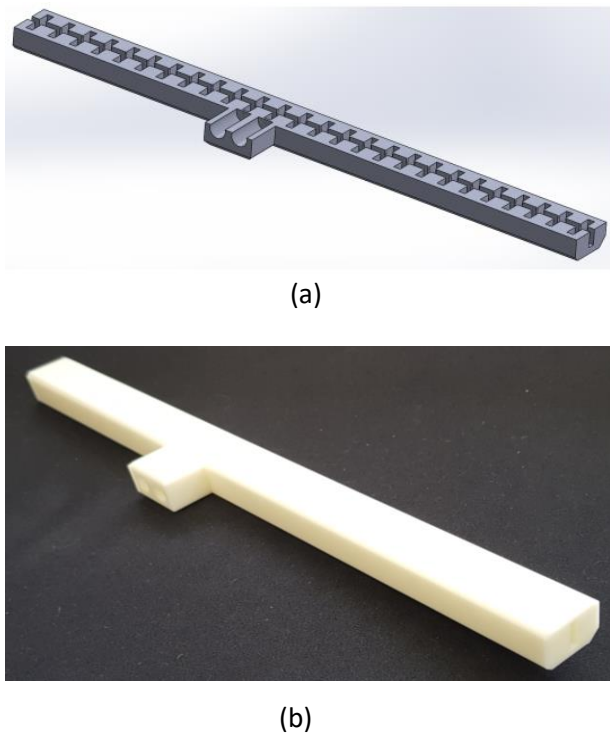


Figure 8: (a) Cross section view of the numerically analyzed sensor, (b) Isometric view of the fabricated sensor

out through another 1 mm-diameter tube until desired concentrations were reached, as confirmed

The number of unit cells sufficient to support a wave with a nearly flat dispersion curve was found to be 26 unit cells, with 15 unit cells between the speaker and the first of the two 8 mm-diameter microphones, and 11 unit cells between the second microphone and the outlet. A larger number of unit-cells would make the sensor too large for the gas chamber, and essentially not necessary. Isometric views of the numerically analyzed and fabricated structure are shown in Figure 8.

The extrusion depth for the 2D design was set to be 12.5 mm and the thickness of the plates representing the hypothetically rigid corrugated surface was set to 3.2 mm. The fabricated upper corrugations corresponding to the locations of the two microphones were covered by 1 mm-thick plates, with a 1 mm-diameter central hole for the sound to get to the head of the microphone positioned against the said 1 mm ceiling. Two microphones constructed as cylinders with flat sound-receptive circular heads, were positioned perpendicularly to the axis of the waveguide, at adjacent unit cells, centered above the vertical corrugations. The cylinders were mounted using plastic nests printed monolithically with the structure.

To perform acoustic measurements, two microphones on cylindrical sticks were inserted into the sockets of the sensor, as depicted in Figure 8, having the air pressure wave reaching them through the 1 mm-diameter hole. A small speaker of an earphone was attached by duct tape to one end of the waveguide, 15 unit-cells distant from the microphone sockets, with the other waveguide end remaining open. The sound was generated using the free software Audacity. Measurements were conducted in a laboratory, using a gas chamber, into which CO_2 was pumped through a 1 mm-diameter tube from a CO_2 balloon, with 0.1 bar relative pressure during the course of approximately 1 minute, until reaching a concentration higher than 10000 ppm, according to a reference commercial optical IR CO_2 -concentration sensor ("Qingping Air Monitor Lite"). Subsequently, a manual air pump was used to pump in air and let the CO_2 -polluted air flow

by the reference sensor. Acoustic measurements were then performed at steady-state concentrations

of 0.7%, 0.5%, 0.3% and 0.1%, in addition to the 0% concentration measurement that had been conducted outside the gas chamber. The experimental setup is shown in Figure 9.



Figure 9: Experimental setup: a PMMA box (with an inlet for gas and an outlet) containing the fabricated sensor, with two microphones inserted in the sockets, an earphone speaker attached by duct tape at the longer end, a soundblaster device Omni Surround 5.1, connecting the three audio devices to the computer outside the chamber using USB ports installed in the chamber, with a piece of polystyrene to support the sensor to have a free outflux, and a reference sensor Qingping Air Monitor Lite.

The measured phases obtained using a procedure discussed in detail in Appendix B, are depicted on top of the calculated values in Figure 10. The concentration for each measurement was read from the reference Qingping Air Monitor. It should be noted that the reference sensor measures total CO_2 concentration using an optical absorption mechanism. Due to this, the monitor of the reference sensor shows the sum of CO_2 in standard air and the additionally pumped CO_2 . To deduce the additionally pumped CO_2 concentration, an amount of 0.04% had to be subtracted. The reason for this is that the computation involved specifying the speed of sound of standard air at a certain temperature, and standard air already contains 0.04% CO_2 .

One can observe excellent correspondence between the measured and calculated concentrations, i.e., between the concentrations measured by the reference sensor and those measured by the proposed sensor. The sensor shows high accuracy

already at volume concentrations as small as 0.04% CO_2 , which is a non-hazardous concentration, while the steep initial rise guarantees good phase resolution even for a small concentration change.

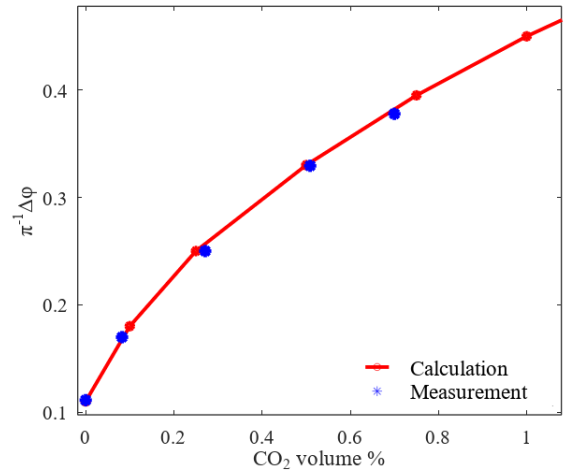


Figure 10: Comparison of the calculated and measured relative phase change versus the concentration of CO_2 .

6. Discussion

The proposed sensor represents a novel sensing platform characterized by high accuracy and sensitivity, low-cost, and the possibility for a rapid and reliable measurement with low maintenance. The major novelty of the proposed sensor is the fundamental sensing principle, which is based on the nearly-flat mode tailored in an ASFS waveguide. In other words, we use a design that adds a perturbation to an otherwise symmetric waveguide, characterized by a perfectly-flat band. The symmetry is broken vertically, in a fashion that maintains the uniformity of the waveguide in the propagation direction, while achieving a nearly-flat mode, similarly to the idea in [62]. This is different from some other designs that introduce horizontal perturbation to achieve a nearly-flat mode [65]-[66]. Horizontal symmetry-breaking enforces fabrication requirements in the propagation direction. When approaching the manufacturing limit for a small-enough perturbation for high-enough sensitivity, the fabrication inaccuracy may destroy the propagating wave, damaging the ability to measure a phase difference as an indication for the concentration, with its advantages in terms of robustness to noise

and efficient measurement time. A vertical perturbation helps to overcome such difficulties.

The majority of the proposed acoustic sensors rely on amplitude measurements, which are more sensitive to noise and require longer or more carefully planned measurement times. This problem was addressed in [44], but only partially. Furthermore, in most of the existing designs, the first acoustic wave mode is employed, which generally corresponds to a non-flat dispersion band, which limits the sensitivity.

Our solution, based on a nearly-flat mode opens up the possibility to employ phase change as the principle for sensing, which is a more robust approach than that based on the change of amplitude, while achieving sensitivity gain. Specifically, when introducing a small vertical perturbation to the symmetric design, the second mode band ceases to be flat for all wavenumbers but remains flat for the zero wavenumber. Therefore, the operational frequency is chosen so that the wavenumber of the second-mode for standard air is equal to zero. Consequently, the wavenumber increases sharply even for infinitesimally small changes in gas concentration, and this provides a highly sensitive phase-concentration response, allowing very high sensing resolution for small concentrations.

When compared to other types of acoustic gas sensors, the proposed design shows some comparable properties as well as some more advantages. The sensitivity of the periodic structure-based sensors as in [53] and [61] are of the order of 10 mHz/ppm, which might be considered similar to the proposed one, but one should note that these sensors employ almost-linear modes and operate at frequencies of 60 kHz, which is 5.4 times higher than the proposed operating frequency. QCM, SAW/BAW, and FBAR sensors typically exhibit sensitivity of tens of Hz/ppm, 10^3 - 10^2 kHz/ppm, and kHz/ppm, while their operating frequencies are in the range 1-10 kHz, 100 kHz – GHz, and 100 MHz – 20 GHz, respectively [49]. Therefore, their sensitivity can be considered as comparable to the proposed one. As for the limit of detection, it is smaller in other

acoustic sensors, however, they are typically aimed at air quality applications.

As previously discussed, our sensitivity is equal to 0.003 Hz/ppm, however, this value should be taken cautiously and interpreted in the context of the given sensing principle. Since the robustly measurable value is phase, we design the sensor such that the phase difference between adjacent unit-cells spans π radians for the maximum relevant CO₂ concentration and the related frequency span is its consequence. Also, the sensor is designed such that the phase-concentration response curve is nonlinear, resembling a square-root function, for which the sensitivity, or the slope, becomes arbitrarily high at low concentrations. Therefore, the smaller the concentrations range the higher the sensitivity value, i.e., the sensitivity can be almost arbitrarily chosen. High sensitivity values are limited only by practical considerations, such as the accuracy of the numerical algorithm of the employed software and the sampling rate of the used electronic equipment.

It was shown that even for small concentrations the proposed sensor is very accurate. Although only the measurements up to 1% concentration have been shown, it should be noted that the proposed sensor can measure concentrations up to 3% or even up to 5% with a slight change in the sensor design. In other words, the proposed sensor can work in a large range of concentrations, without reaching saturation and as such be applied in various industrial applications. In comparison to other acoustic sensors, which typically require advanced fabrication processes, the proposed sensor can be printed from cheap PLA material and requires only an earphone and two microphones, the signals from which can be coordinated by a simple electronic board and analyzed using a standard microprocessor. In addition to these advanced properties, the sensor has shorter measurement time in comparison to others, it is label-free, provides rapid and robust response, and does not require relaxation time or air flushing.

Since the basic detection mechanism is related to molecular weight of a gas, the sensor is equivalently operative for detection of any heavy gas, such as

N_2O , C_3H_8 , C_4H_{10} or light gas such as CH_4 or NH_3 . At the same time, this represents an obstacle for the sensor's selectivity since several gases can have (approximately) the same molecular weight.

7. Conclusions

In this work, we have investigated an ASFS waveguide and its application in gas sensing. First, a numerical method was suggested for robust dispersion analysis based on the expansion of the acoustic fields in the direction perpendicular to the wave propagation direction, using a basis of wave functions, but employing a point-collocation rather than mode-matching technique. The method showed satisfactory results coinciding with finite element analysis implemented in the commercial software COMSOL-Multiphysics. An ASFS waveguide was fabricated using 3D printing technology and its responses were measured in a simple measurement setup that includes off-the-shelf microphones and a speaker. The measurement results showed excellent agreement with the calculated ones.

Furthermore, it was numerically demonstrated how the second mode of an ASFS waveguide that has nearly-flat nature can be used for gas sensing purposes. Consequently, a numerically-optimized CO_2 sensor was fabricated using 3D printing technology and experimentally tested in a gas chamber controlled CO_2 concentration. The measured results matched well to the calculated ones, demonstrating the potential of the proposed sensor. Besides the novelty of the sensing principle, the sensor is characterized by high sensitivity, accuracy, low costs, robustness to noises, rapid response without the need for relaxation time and maintenance, and the possibility to operate in a large range of concentrations without reaching saturation. Consequently, we opt that the proposed work represents a valuable contribution not only to the theoretical analysis of acoustic periodic structures but also to sensor engineering applicable for real-world problems.

Acknowledgements

The work described in this paper is conducted within the project NOCTURNO, which receives funding from

the European Union's Horizon 2020 research and innovation programme under Grant No. 777714. This work is also supported through the ANTARES project that has received funding from the European Union's Horizon 2020 research and innovation programme under grant agreement SGA-CSA No. 739570 under FPA No. 664387, <https://doi.org/10.3030/739570>.

The work was also supported by the Department of Defense, the Air Force Office of Scientific Research, and the Simons Foundation.

Appendix A: Derivation of the calculated dispersion diagram for the asymmetric spoof-fluid-spoof waveguide

The basic governing equations of a fluid subjected to acoustic excitation are as follows:

$$\begin{aligned} \rho \ddot{\mathbf{v}} &= -\nabla p, \dot{\rho} + \rho \nabla \cdot \mathbf{v} = 0, \frac{\partial p}{\partial \rho} = \\ c^2, \nabla \times \mathbf{v} &= 0 \Rightarrow \nabla^2 p = \frac{1}{c^2} \frac{\partial^2 p}{\partial t^2}, \nabla^2 \mathbf{v} = \\ \frac{1}{c^2} \frac{\partial^2 \mathbf{v}}{\partial t^2}. \end{aligned} \quad (\text{A.1})$$

In frequency space the following relations hold:

$$\begin{aligned} \nabla^2 \check{p} + k^2 \check{p} &= 0, \nabla^2 \check{\mathbf{q}} + k^2 \check{\mathbf{q}} = \\ 0, \nabla \check{p} &= k \check{\mathbf{q}}, \nabla \cdot \check{\mathbf{q}} = k \check{p}, \end{aligned} \quad (\text{A.2})$$

where

$$\begin{aligned} \hat{p} &= e^{-i\omega t} p, \hat{\mathbf{v}} = e^{-i\omega t} \mathbf{v}, k = \frac{\omega}{c}, \eta = \\ \rho c, \hat{\mathbf{q}} &= \eta \hat{\mathbf{v}}, \hat{\mathbf{q}} = -i \check{\mathbf{q}}, \hat{p} = -i \check{p}, \end{aligned} \quad (\text{A.3})$$

and where ρ , p , c , \mathbf{v} , ω are the density, pressure, speed of sound, material velocity and excitation frequency in the fluid, respectively.

It is next assumed that the excitation is uniform in the z direction, and consequently, so is the response. Therefore, the following equations are assumed to hold in the x - y plane:

$$\begin{aligned} \frac{\partial^2 \check{p}}{\partial x^2} + \frac{\partial^2 \check{p}}{\partial y^2} + k^2 \check{p} &= 0, q_x = \\ k^{-1} \frac{\partial \check{p}}{\partial x}, q_y &= k^{-1} \frac{\partial \check{p}}{\partial y}. \end{aligned} \quad (\text{A.4})$$

The general solution of the Eq. (A.4) is

$$\check{p}(x, y, z) = \check{p}(x, y) = \sum_m \left[(A_m e^{-ik_{x,m}x} + B_m e^{ik_{x,m}x}) e^{-i\sqrt{k^2 - k_{x,m}^2}y} + (C_m e^{-ik_{x,m}x} + D_m e^{ik_{x,m}x}) e^{i\sqrt{k^2 - k_{x,m}^2}y} \right] \quad (A.5)$$

A wave solution (with $k_{x,m} \in \mathbb{R}$) would be supported for waves with small enough wavelength, namely, $k_{x,m} \gg x_{max}^{-1}$. It is further assumed that, for any value of z , the fluid occupies in the x - y plane some subspace bounded by straight-segment boundaries as depicted in Figure 1.

One can then specify the coefficients A, B, C, D, k_x in each of the three sub-domains in a unit cell of horizontal length d . In the domains I and III the condition of vanishing normal velocity on each of the three rigid boundaries produces the following solutions:

$$\check{p}^{III}(x, y) = \frac{1}{a_3} \sum_{m=0}^{\infty} A_m^{III} \frac{\cos(m\pi x/a_3) \cos[\sqrt{k^2 - (m\pi/a_3)^2}(\frac{g}{2} + h_3 - y)]}{\sqrt{k^2 - (m\pi/a_3)^2} \cos(\sqrt{k^2 - (m\pi/a_3)^2} h_3)}, \quad (A.6)$$

where the coefficients A_m^{III} are to be determined by requiring that $\check{p}^{III}(x, g/2) = \check{p}^{II}(x, g/2)$.

$$\check{p}^I(x, y) = \frac{1}{a_1} \sum_{m=0}^{\infty} A_m^I \frac{\cos(m\pi x/a_1) \cos[\sqrt{k^2 - (m\pi/a_1)^2}(\frac{g}{2} + h_1 + y)]}{\sqrt{k^2 - (m\pi/a_1)^2} \cos(\sqrt{k^2 - (m\pi/a_1)^2} h_1)}, \quad (A.7)$$

and the coefficients A_m^I are to be determined by requiring that $\check{p}^I(x, -g/2) = \check{p}^{II}(x, -g/2)$.

The horizontal boundary conditions in domain I and III impose $a_{1,3}$ -periodicity on the solution, since the normal velocities have to be equal and vanishing at both $x = 0$ and $x = a_{1,3}$. In contrast, in the middle layer there are no horizontal boundary conditions, and thus for a given wave with its given wavelength, the phase difference between $x = 0$ and $x = d$ would generally be non-vanishing. Hence, the solution in domain II will not be d -periodic in x , but at best d -periodic up to a phase shift.

For every value of y , for x -periodic waveguides, the spectral wave-equation is linear second-order in x with no first derivative and with periodic coefficients, which makes it a Hill equation. For the Hill equation a Floquet-theory result exists [77] according to which the solution is d -periodic up to a phase shift, namely, that $dk_{x,m} = 2m\pi + \Delta_d \phi, m \in \mathbb{Z}$. Thus, one has

$$\check{p}^{II}(x, y) = \frac{1}{d} \sum_{m=-\infty}^{\infty} \frac{e^{-i(m + \frac{\Delta_d \phi}{2\pi}) \frac{2\pi}{d} x}}{\sqrt{k^2 - [(m + \frac{\Delta_d \phi}{2\pi}) \frac{2\pi}{d}]^2}} \times \left\{ A_m^{II} e^{-i\sqrt{k^2 - [(m + \frac{\Delta_d \phi}{2\pi}) \frac{2\pi}{d}]^2} y} + B_m^{II} e^{i\sqrt{k^2 - [(m + \frac{\Delta_d \phi}{2\pi}) \frac{2\pi}{d}]^2} y} \right\}, \quad (A.8)$$

where $\Delta_d \phi \in [0, 2\pi)$ is the phase shift over distance d of a wave with a given frequency ω . The coefficients $A_{\pm|m|}^{II}, B_{\pm|m|}^{II}$ would be determined by the requirement to comply with the vanishing of q_y at the vertical boundaries at $a_3 < x < d, y = g/2$ and $a_1 < x < d, y = -g/2$, and with continuity of normal velocities, namely, $\eta^{-1} q_y$ at $0 < x < a_3, y = g/2$ and $0 < x < a_1, y = -g/2$.

If the waveguide is comprised of N_d unit cells, then it would support wave solutions with wavelength satisfying the condition $\Delta_d \phi \gg N_d^{-1}$. For example, for $N_d = 15$, adopting that $10 \gg 1$, one could have waves for $\frac{\Delta_d \phi}{\pi} > 0.2$. Due to the symmetry with respect to the sign of x , the relevant range of normalized wavenumbers for the said example would be $\frac{\Delta_d \phi}{\pi} \in [0.2, 1]$. The said symmetry would also render the group velocity very low for $\frac{\Delta_d \phi}{\pi} > 0.8$. Consequently, one would be able to observe waves in the wavelength range of $\frac{\Delta_d \phi}{\pi} \in [0.2, 0.8]$. The smallest possible wavelength in a d -periodic waveguide is d , so shorter waves will not propagate. The largest wavelength for propagating waves would be, as aforesaid, of wavelength around $0.1N_d d$. Consequently, a dispersion study is only possible for $N_d > 10$.

For the possibility of a numerical solution of the collocation type, the x coordinate in the range $(0, d]$ is divided as uniformly as possible into segments, or rather a set of discrete points is chosen in the said range, with as uniform distances as possible between them, to enforce the boundary conditions. More specifically, at $y = g/2$, the segment $0 < x < a_3$ is divided into n_{a_3} uniformly spaced points, and the segment $a_3 < x < d$ is divided into n_{s_3} uniformly spaced points. Similarly, at $y = -g/2$, the segment $0 < x < a_1$ is divided into n_{a_1} uniformly spaced points, and the segment $a_1 < x < d$ is divided into n_{s_1} uniformly spaced points.

The stability of this spectral collocation method is guaranteed for the following choice of parameters:

$$n_{s_{1,3}} = \begin{cases} \left\lceil \frac{d-a_{1,3}}{a_{1,3}} n_{a_{1,3}} \right\rceil, & \text{if } \left\lceil \frac{d-a_{1,3}}{a_{1,3}} n_{a_{1,3}} \right\rceil \text{ is even} \\ \left\lceil \frac{d-a_{1,3}}{a_{1,3}} n_{a_{1,3}} \right\rceil + 1, & \text{if } \left\lceil \frac{d-a_{1,3}}{a_{1,3}} n_{a_{1,3}} \right\rceil \text{ is odd} \end{cases} \quad (\text{A.9})$$

where $\lceil \cdot \rceil$ is the ceiling function, or the closest larger integer number.

In addition, the infinite series have to be truncated in numerical calculations. The upper limit of infinity in the given solutions is hence replaced by N_I , N_{II} , and N_{III} . In order to extract unambiguously the $N_{III} + 1$ coefficients $A_m^{I,II}$ from equating the pressure in domains I and III at the $n_{a_{1,3}}$ collocation points to the pressure at domain II at the same points, the following relations must hold:

$$n_{a_{1,3}} = N_{I,III} + 1. \quad (\text{A.10})$$

Finally, for the number of equations to correspond to the number of unknown coefficients, the following relation must hold:

$$N_{II} = \frac{1}{4} (2n_{a_1} + 2n_{a_3} + n_{s_1} + n_{s_3} - N_I - N_{III} - 4). \quad (\text{A.11})$$

Furthermore, symmetry between the lower and upper boundaries requires that $n_{a_1} + n_{s_1} = n_{a_3} + n_{s_3}$. Consequently, if this requirement is satisfied, the following relation would hold: $2N_{II} = N_I +$

$n_{s_1} = N_{III} + n_{s_3}$. Since n_{s_3} is even, a necessary condition is that N_I be even, and that N_{III} would satisfy the relation

$$N_{III} + n_{s_3} = N_I + n_{s_1}. \quad (\text{A.12})$$

This means that there is only one free parameter in this algorithm, namely, N_I , which can be an arbitrary even integer. The chosen value should be large enough with respect to unity to obtain convergence, but not too large to avoid resonance with numerical noise. In the solved examples the choice $N_I = 10$ was made.

An important remark should be made here. The differential equation (A.4) is smooth in each smooth-boundary domain, and thus its solution is smooth. Therefore, the Fourier coefficients of the solution should decay exponentially in domains I and III and they are proportional to A_m^I, A_m^{III} . In domain II, the solution is a Fourier series in x , multiplied by a low frequency oscillatory function of x . Consequently, the solution would not contain highly oscillatory large amplitude modes. Thus, enforcing continuity at a large number of collocation points will guarantee *small* field discontinuities between the collocation points, since the solutions would not be able to oscillate with a large amplitude between them. Therefore, in this case, the collocation method of enforcing continuity at interfaces is expected to be reliable and convergent.

Writing down the continuity equations for pressure and vertical velocity at $0 < x < a_3$, $y = g/2$ and $0 < x < a_1$, $y = -g/2$ and the condition of vanishing vertical velocities at $a_3 < x < d$, $y = g/2$ and $a_1 < x < d$, $y = -g/2$ one obtains a system of 6 sets of equations for 6 sets of variables $(\mathbf{w} = \{A_m^I, A_{\pm|m|}^{II}, B_{\pm|m|}^{II}, A_m^{III}\}^T)$. Obtaining the representative matrix \mathbf{H} of this system of equations, namely, $\mathbf{H}\mathbf{w} = 0$, requires only the substitution of a set of uniformly spaced points in each segment x , namely,

$$\begin{aligned} x \rightarrow \{x\}_j, x_j^{(a_1, a_3)} &= \frac{a_{1,3}}{n_{a_{1,3}} + 1} j, j = \\ 1, 2, \dots, n_{a_{1,3}}, x_j^{(s_1, s_3)} &= a_{1,3} + \frac{d - a_{1,3}}{n_{a_{1,3}} + 1} j, j = \\ 1, 2, \dots, n_{a_{1,3}}. \end{aligned} \quad (\text{A.13})$$

After the matrix \mathbf{H} is constructed, with each column corresponding to a mode of the solution in the entire domain and each row corresponding to an equation on a collocation point, numerical eigenvalue analysis of \mathbf{H} is performed and the eigenvalue with the minimum absolute value is identified.

Nonzero-amplitude pressure waves can be supported by the studied system only for a vanishing minimum absolute-value eigenvalue of \mathbf{H} . The logarithm of this measure is plotted against the wave frequency for $\Delta_d\phi = \pi/2$ for the following geometrical parameters $d = 34.3$ mm, $a_1 = a_3 = g = 10.3$ mm, $h_1 = 20.6$ mm, $h_3 = 18.2$ mm, $c = 346.87$ m/s², $\rho = 1.1802$ kg/m³ in Figure A.1.

For high enough frequency resolution and spatial resolution, the narrow dips as shown in Figure A.1 would approach minus infinity and the corresponding frequencies would be the nonzero-amplitude wave frequencies for the assumed value of $\Delta_d\phi$.

In order to obtain the wavenumber for a given frequency, one has to measure the phases of the propagating pressure waves at two locations in the waveguide with a distance d between them.

If one acknowledges a relative error δ in the distance between two probes measuring the pressure, rendering the actual said distance to be $(1+\delta)d$, then modes corresponding to terms with $m = \mathcal{O}(|\delta^{-1}|)$ may produce additional parasitic finite phase shift.

However, for such terms the denominator in Eq. (A.8) would be of the order of $m = \mathcal{O}(|\delta^{-1}|) \gg 1$, rendering the contribution of the term insignificant.

The latter would hold due to the fact that the coefficients A_m^{II}, B_m^{II} decay exponentially for $m \gg 1$, balancing the braced expression to order of unity for $y = g/2$. This analysis shows that the pressure is stable with respect to phase-shift measurement at the waveguide boundaries. The coefficients may decrease even more strongly, but not more weakly, as the alternating harmonic series is already marginally convergent.

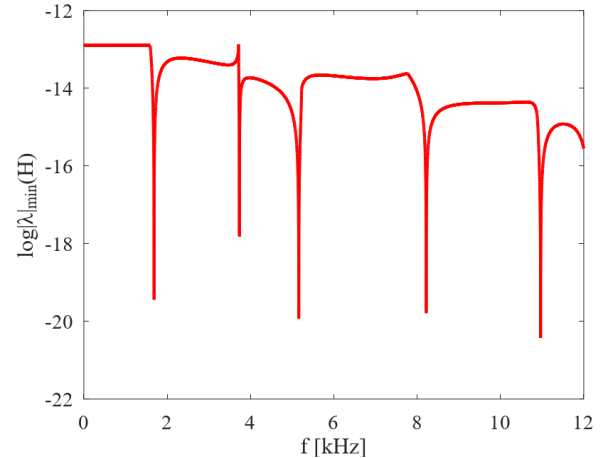


Figure A.1: Plot of $\log|\lambda|_{min}(\mathbf{H})$ vs. $f = \frac{\omega}{2\pi}$.

Appendix B: Details concerning the derivation of the measured dispersion diagram

In order to determine the phase shift between the signals measured by the two microphones placed one unit-cell apart, one has to establish the correct time-instance for the comparison. For measuring this time-instance one should start the clock at a certain moment. The appropriate moment for starting the said clock is when the amplitude of the signal in the microphones becomes sufficiently higher than numerical noise.

The time period between the aforementioned moment and the sought time-instance for comparison can be calculated as follows. The time interval between start of rise and correct instance for phase comparison should be given by the distance from the speaker to the microphones, divided by the phase velocity. The phase velocity obviously depends on the phase. The question is what phase should be taken for this calculation. It is opted here that this phase should be related to the phase difference to be measured at the aforementioned time-instance for comparison. In this sense it is an iterative process. First, the wavenumber should be assumed (in relative-phase units). One can either just assume any number and repeat the process several times until convergence is reached. A shorter path is assuming the right wavenumber using the numerical

dispersion diagram and the operational frequency. Using the theoretical diagram can only shorten the iterative process, by producing a better initial guess, but even without it the iterative process will converge. This is to say that the procedure is by no means one of cyclic logic.

Since the dependence of the phase difference on the right time instance for comparison is weak, when taking the initial guess for the wavenumber based on the computational plot, two iterations are sufficient.

Also, to be sure that the correct phase arrives at the microphone, the slowest velocity should be taken, i.e., the one corresponding to the largest wavenumber when choosing from the two symmetric values $\Delta\phi$ and $2\pi - \Delta\phi$. Since in the chosen approach, due to symmetry, one has $\Delta\phi \in (0, \pi]$, the maximum wavenumber would always be $(2\pi - \Delta\phi)/d$, where d is the periodicity. Therefore,

$$\Delta t_\phi = \frac{\Delta L}{\frac{\omega d}{2\pi - \Delta\phi}} \quad (\text{B.1})$$

References

1. J. W. S. Rayleigh, *The Theory of Sound*, (Dover, New York, 1945).
2. L. Brillouin, *Wave Propagation in Periodic Structures* (Dover, New York, 1946).
3. M. M. Sigalas and E. N. Economou, *Elastic and Acoustic Wave Band Structure*, *Journal of Sound and Vibration* 158, 377 (1992).
4. M. S. Kushwaha, P. Halevi, L. Dobrzynski, and B. Djafari-Rouhani, *Acoustic Band Structure of Periodic Elastic Composites*, *Phys. Rev. Lett.* 71, 2022 (1993).
5. M. S. Kushwaha, *Classical Band Structure of Periodic Elastic Composites*, *Int. J. Mod. Phys. B* 10, 977 (1996).
6. Z. Liu, X. Zhang, Y. Mao, Y. Y. Zhu, Z. Yang, C. T. Chan, and P. Sheng, *Locally Resonant Sonic Materials*, *Science* 289, 1734 (2000).
7. M. I. Hussein, M. J. Leamy, and M. Ruzzene, *Dynamics of Phononic Materials and Structures: Historical Origins, Recent Progress, and Future Outlook*, *Applied Mechanics Reviews* 66, 040802 (2014).
8. S. A. Cummer, J. Christensen, and A. Alù, *Controlling Sound with Acoustic Metamaterials*, *Nat Rev Mater* 1, 16001 (2016).
9. J. B. Pendry, L. Martín-Moreno, and F. J. García-Vidal, *Mimicking Surface Plasmons with Structured Surfaces*, *Science* 305, 847 (2004).
10. S. A. Maier, S. R. Andrews, L. Martín-Moreno, and F. J. García-Vidal, *Terahertz Surface Plasmon-Polariton Propagation and Focusing on Periodically Corrugated Metal Wires*, *Phys. Rev. Lett.* 97, 176805 (2006).
11. K. Song and P. Mazumder, *Active Terahertz Spoof Surface Plasmon Polariton Switch Comprising the Perfect Conductor Metamaterial*, *IEEE Trans. Electron Devices* 56, 2792 (2009).
12. M. A. Kats, D. Woolf, R. Blanchard, N. Yu, and F. Capasso, *Spoof Plasmon Analogue of Metal-Insulator-Metal Waveguides*, *Opt. Express* 19, 14860 (2011).
13. X. Shen, T. J. Cui, D. Martin-Cano, and F. J. García-Vidal, *Conformal Surface Plasmons Propagating on Ultrathin and Flexible Films*, *Proc. Natl. Acad. Sci. U.S.A.* 110, 40 (2012).
14. Z. Ma, S. M. Hanham, P. Arroyo Huidobro, Y. Gong, M. Hong, N. Klein, and S. A. Maier, *Terahertz Particle-in-Liquid Sensing with Spoof Surface Plasmon Polariton Waveguides*, *APL Photonics* 2, 116102 (2017).
15. L. Ye, H. Feng, G. Cai, Y. Zhang, B. Yan, and Q. H. Liu, *High-Efficient and Low-Coupling Spoof Surface Plasmon Polaritons Enabled by V-Shaped Microstrips*, *Opt. Express* 27, 22088 (2019).
16. C. H. Wu, L. Shen, H. Zhang, J. Yan, D. J. Hou, G. Zhou, and Y. L. Wu, *Equivalent Circuit Parameters of Planar Transmission Lines with Spoof Surface Plasmon Polaritons and*

Its Application in High Density Circuits, *Sci Rep* 9, 18853 (2019).

- 17. J. Christensen, P. A. Huidobro, L. Martín-Moreno, and F. J. García-Vidal, Confining and Slowing Airborne Sound with a Corrugated Metawire, *Appl. Phys. Lett.* 93, 083502 (2008).
- 18. Z. He, H. Jia, C. Qiu, Y. Ye, R. Hao, M. Ke, and Z. Liu, Nonleaky Surface Acoustic Waves on a Textured Rigid Surface, *Phys. Rev. B* 83, 132101 (2011).
- 19. L. Quan, F. Qian, X. Liu, X. Gong, and P. A. Johnson, Mimicking Surface Plasmons in Acoustics at Low Frequency, *Phys. Rev. B* 92, 104105 (2015).
- 20. O. Schnitzer, Spoof Surface Plasmons Guided by Narrow Grooves, *Phys. Rev. B* 96, 085424 (2017).
- 21. W. K. Cao, L. T. Wu, C. Zhang, G. Y. Song, J. C. Ke, Q. Cheng, and T. J. Cui, Acoustic Surface Waves on Three-Dimensional Groove Gratings with Sub-Wavelength Thickness, *Appl. Phys. Express* 11, 087301 (2018).
- 22. J. Christensen, A. I. Fernandez-Dominguez, F. de Leon-Perez, L. Martin-Moreno, and F. J. Garcia-Vidal, Collimation of Sound Assisted by Acoustic Surface Waves, *Nature Phys* 3, 851 (2007).
- 23. J. Christensen, L. Martín-Moreno, and F. J. García-Vidal, Enhanced Acoustical Transmission and Beaming Effect through a Single Aperture, *Phys. Rev. B* 81, 174104 (2010).
- 24. N. Korozlu, O. A. Kaya, A. Cicek, and B. Ulug, Self-Collimation and Slow-Sound Effect of Spoof Surface Acoustic Waves, *Journal of Applied Physics* 125, 074901 (2019).
- 25. S. Xie, S. Ouyang, Z. He, X. Wang, K. Deng, and H. Zhao, Bending and Splitting of Spoof Surface Acoustic Waves through Structured Rigid Surface, *Results in Physics* 8, 52 (2018).
- 26. Y. Zhou, M.-H. Lu, L. Feng, X. Ni, Y.-F. Chen, Y.-Y. Zhu, S.-N. Zhu, and N.-B. Ming, Acoustic Surface Evanescent Wave and Its Dominant Contribution to Extraordinary Acoustic Transmission and Collimation of Sound, *Phys. Rev. Lett.* 104, 164301 (2010).
- 27. A. Climente, D. Torrent, and J. Sánchez-Dehesa, Sound Focusing by Gradient Index Sonic Lenses, *Appl. Phys. Lett.* 97, 104103 (2010).
- 28. Y. Ye, M. Ke, Y. Li, T. Wang, and Z. Liu, Focusing of Spoof Surface-Acoustic-Waves by a Gradient-Index Structure, *Journal of Applied Physics* 114, 154504 (2013).
- 29. T. Liu, F. Chen, S. Liang, H. Gao, and J. Zhu, Subwavelength Sound Focusing and Imaging Via Gradient Metasurface-Enabled Spoof Surface Acoustic Wave Modulation, *Phys. Rev. Applied* 11, 034061 (2019).
- 30. L. T. Wu, G. Y. Song, W. K. Cao, Q. Cheng, T. J. Cui, and Y. Jing, Generation of Multiband Spoof Surface Acoustic Waves via High-Order Modes, *Phys. Rev. B* 97, 214305 (2018).
- 31. J. Zhu, Y. Chen, X. Zhu, F. J. Garcia-Vidal, X. Yin, W. Zhang, and X. Zhang, Acoustic Rainbow Trapping, *Sci Rep* 3, 1728 (2013).
- 32. N. Janković, S. Ilić, V. Bengin, S. Birgermajer, V. Radonić, and A. Alù, Acoustic Spoof Surface Plasmon Polaritons for Filtering, Isolation and Sensing, *Results in Physics* 28, 104645 (2021).
- 33. N. Cselyuszka, A. Alù, and N. Janković, Spoof-Fluid-Spoof Acoustic Waveguide and Its Applications for Sound Manipulation, *Phys. Rev. Applied* 12, 054014 (2019).
- 34. X. Huang, Z. Gong, and Y. Lv, Advances in Metal-Organic Frameworks-Based Gas Sensors for Hazardous Substances, *TrAC Trends in Analytical Chemistry* 153, 116644 (2022).
- 35. R. Jana, S. Hajra, P. M. Rajaitha, K. Mistewicz, and H. J. Kim, Recent Advances in Multifunctional Materials for Gas Sensing Applications, *Journal of Environmental Chemical Engineering* 10, 108543 (2022).

36. S. Dhall, B. R. Mehta, A. K. Tyagi, and K. Sood, A Review on Environmental Gas Sensors: Materials and Technologies, *Sensors International* 2, 100116 (2021).

37. J. Zhu, H. Wen, Y. Fan, X. Yang, H. Zhang, W. Wu, Y. Zhou, and H. Hu, Recent Advances in Gas and Environmental Sensing: From Micro/Nano to the Era of Self-Powered and Artificial Intelligent (AI)-Enabled Device, *Microchemical Journal* 181, 107833 (2022).

38. T. Seesaard, N. Goel, M. Kumar, and C. Wongchoosuk, Advances in Gas Sensors and Electronic Nose Technologies for Agricultural Cycle Applications, *Computers and Electronics in Agriculture* 193, 106673 (2022).

39. N. Nasiri and C. Clarke, Nanostructured Gas Sensors for Medical and Health Applications: Low to High Dimensional Materials, *Biosensors* 9, 43 (2019).

40. L. Zipser and F. Wächter, Acoustic Sensor for Ternary Gas Analysis, *Sensors and Actuators B: Chemical* 26, 195 (1995).

41. L. Zipser, F. Wächter, and H. Franke, Acoustic Gas Sensors Using Airborne Sound Properties, *Sensors and Actuators B: Chemical* 68, 162 (2000).

42. K. Keeratirawee and P. C. Hauser, Determination of Binary Gas Mixtures by Measuring the Resonance Frequency in a Piezoelectric Tube, *Sensors* 22, 1691 (2022).

43. European Patent 1325319, B. Hök, Int. Class. GO1N29/02, Appl. No. 01975104, EP-09.07.2003, Acoustic CO₂-sensor.

44. United States Patent 9869659B2, J.R. Buckland and A.R. Campbell, Int. Class. GO1N29/02, GO1N29/036, Acoustic Sensor, 16 Jan. 2018.

45. D. B. Go, M. Z. Atashbar, Z. Ramshani, and H.-C. Chang, Surface Acoustic Wave Devices for Chemical Sensing and Microfluidics: A Review and Perspective, *Anal. Methods* 9, 4112 (2017).

46. K. Länge, Bulk and Surface Acoustic Wave Sensor Arrays for Multi-Analyte Detection: A Review, *Sensors* 19, 5382 (2019).

47. F. Fauzi, A. Rianjanu, I. Santoso, and K. Triyana, Gas and Humidity Sensing with Quartz Crystal Microbalance (QCM) Coated with Graphene-Based Materials – A Mini Review, *Sensors and Actuators A: Physical* 330, 112837 (2021).

48. M. P. Nair, A. J. T. Teo, and K. H. H. Li, Acoustic Biosensors and Microfluidic Devices in the Decennium: Principles and Applications, *Micromachines* 13, 24 (2021).

49. A. Kumar and R. Prajesh, The Potential of Acoustic Wave Devices for Gas Sensing Applications, *Sensors and Actuators A: Physical* 339, 113498 (2022).

50. Q. Zhou, C. Zheng, L. Zhu, and J. Wang, A Review on Rapid Detection of Modified Quartz Crystal Microbalance Sensors for Food: Contamination, Flavour and Adulteration, *TrAC Trends in Analytical Chemistry* 157, 116805 (2022).

51. D. Mandal and S. Banerjee, Surface Acoustic Wave (SAW) Sensors: Physics, Materials, and Applications, *Sensors* 22, 820 (2022).

52. O. A. Kaya, N. Korozlu, D. Trak, Y. Arslan, and A. Cicek, One-Dimensional Surface Phononic Crystal Ring Resonator and Its Application in Gas Sensing, *Appl. Phys. Lett.* 115, 041902 (2019).

53. A. Cicek, D. Trak, Y. Arslan, N. Korozlu, O. A. Kaya, and B. Ulug, Ultrasonic Gas Sensing by Two-Dimensional Surface Phononic Crystal Ring Resonators, *ACS Sens.* 4, 1761 (2019).

54. Y. Pennec, Y. Jin, and B. Djafari-Rouhani, Phononic and Photonic Crystals for Sensing Applications, *Advances in Applied Mechanics* 105 (2019).

55. A. Mehaney and A. M. Ahmed, Theoretical Design of Porous Phononic Crystal Sensor for Detecting CO₂ Pollutions in Air, *Physica E: Low-Dimensional Systems and Nanostructures* 124, 114353 (2020).

56. S. E. Zaki, A. Mehaney, H. M. Hassanein, and A. H. Aly, Fano Resonance Based Defected 1D Phononic Crystal for Highly Sensitive Gas Sensing Applications, *Sci Rep* 10, 17979 (2020).

57. H. Imanian, M. Noori, and A. Abbasiyan, Highly Efficient Gas Sensor Based on Quasi-Periodic Phononic Crystals, *Sensors and Actuators B: Chemical* 345, 130418 (2021).

58. S. E. Zaki and M. A. Basyooni, Ultra-Sensitive Gas Sensor Based Fano Resonance Modes in Periodic and Fibonacci Quasi-Periodic Pt/PtS₂ Structures, *Sci Rep* 12, 9759 (2022).

59. H. Imanian, M. Noori, and A. Abbasiyan, A Highly Efficient Fabry-Perot Based Phononic Gas Sensor, *Ultrasonics* 124, 106755 (2022).

60. Z. A. Zaky, S. Alamri, E. I. Zohny, and A. H. Aly, Simulation Study of Gas Sensor Using Periodic Phononic Crystal Tubes to Detect Hazardous Greenhouse Gases, *Sci Rep* 12, 21553 (2022).

61. A. Cicek, Y. Arslan, D. Trak, F. C. Okay, O. A. Kaya, N. Korozlu, and B. Ulug, Gas Sensing through Evanescent Coupling of Spoof Surface Acoustic Waves, *Sensors and Actuators B: Chemical* 288, 259 (2019).

62. N. Perchikov, O.V. Gendelman, Nonlinear dynamics of hidden modes in a system with internal symmetry, *Journal of Sound and Vibration* 377:185-215 (2016)

63. D. Leykam, A. Andrianov, and S. Flach, Artificial Flat Band Systems: From Lattice Models to Experiments, *Advances in Physics: X* 3, 1473052 (2018).

64. J.G. Beadle T.A. Starkey, J.A. Dockrey, J.R. Sambles and A.P. Hibbins, The acoustic phase resonances and surface waves supported by a compound rigid grating, *Nature Scientific Reports* 8: 10701 (2018)

65. M. Wang, W. Zhou, L. Bi, C. Qiu, M. Ke and Z. Liu, Valley-locked waveguide transport in acoustic heterostructures, *Nature communications* 11: 3000 (2020)

66. D.B. Moore, G.P. Ward, J.D. Smith, A.P. Hibbins, J.R. Sambles and T. a. Starkey, Confined acoustic line modes within a glide symmetric waveguide, *Nature Scientific Reports* 1: 10954 (2022)

67. A. Shakeri, S. Darbari, and M. K. Moravvej-Farshi, Designing a Tunable Acoustic Resonator Based on Defect Modes, Stimulated by Selectively Biased PZT Rods in a 2D Phononic Crystal, *Ultrasonics* 92, 8 (2019).

68. T. Liu, L.-L. Xu, H. Liu, Y.-X. Fan, and Z.-Y. Tao, Manipulation of Acoustic Localizations Based on Defect Mode Coupling in a Corrugated Waveguide, *AIP Advances* 10, 095109 (2020).

69. A. Biçer, M. Günay, N. Korozlu, and A. Cicek, Continuously Tunable Acoustic Fano Resonance in Side-Coupled Helmholtz Resonator Array Assisted by a Surface Phononic Crystal, *Appl. Phys. Lett.* 120, 011902 (2022).

70. C. Sun, A. Song, Z. Liu, Y. Xiang, and F.-Z. Xuan, Topological Fano Resonance of Symmetric Lamb Wave Induced by Antisymmetric Trapped Mode, *AIP Advances* 13, 025008 (2023).

71. D. Reyes D. Martinez, M. Mayorga, H. Heo, E. Walker and A. Neogi, Optimization of the spatial configuration of local defects in phononic crystals for high Q Cavity, *Front. Mech. Eng.* 23(6):592787 (2020)

72. R. J. Astley, FE Mode-Matching Schemes for the Exterior Helmholtz Problem and Their Relationship to the FE-DtN Approach, *Commun. Numer. Meth. Engng.* 12, 257 (1996).

73. R. Kirby and J. B. Lawrie, A Point Collocation Approach to Modelling Large Dissipative Silencers, *Journal of Sound and Vibration* 286, 313 (2005).

74. O. C. Zienkiewicz, R. L. Taylor and J.Z. Zhu, *The Finite Element Method: Its Basis and Fundamentals*, Butterworth-Heinemann (2013).

75. G. Valerio, F. Ghasemifard, Z. Sipus, and O. Quevedo-Teruel, Glide-Symmetric All-Metal

Holey Metasurfaces for Low-Dispersive Artificial Materials: Modeling and Properties, *IEEE Trans. Microwave Theory Techn.* 66, 3210 (2018).

- 76. <https://www.audacityteam.org>
- 77. Floquet, G. (1883). Sur les équations différentielles linéaires. *Ann. ENS* [2], 12(1883):47–88.